RSC Advances

PAPER

View Article Online
View Journal | View Issue

Cite this: *RSC Adv.*, 2019, **9**, 24489

A novel n-type CdS nanorods/p-type $LaFeO_3$ heterojunction nanocomposite with enhanced visible-light photocatalytic performance

Akram-Alsadat Hoseini, Saeed Farhadi,* Abedin Zabardasti and Firouzeh Siadatnasab

In this work, a novel n-type CdS nanorods/p-type $LaFeO_3$ (CdS NRs/LFO) nanocomposite was prepared, for the first time, *via* a facile solvothermal method. The as-prepared n-CdS NRs/p-LFO nanocomposite was characterized by using powder X-ray diffraction (XRD), Fourier transform infrared spectroscopy (FT-IR), X-ray photoelectron spectroscopy (XPS), scanning electron microscopy (SEM), high-resolution transmission electron microscopy (HR-TEM), energy-dispersive X-ray spectroscopy (EDX), UV-visible diffuse reflection spectroscopy (DRS), vibrating sample magnetometry (VSM), photoluminescence (PL) spectroscopy, and Brunauer–Emmett–Teller (BET) surface area analysis. All data revealed the attachment of the LFO nanoparticle on the surface of CdS NRs. This novel nanocomposite was applied as a novel visible light photocatalyst for the degradation of methylene blue (MB), rhodamine B (RhB) and methyl orange (MO) dyes under visible-light irradiation. Under optimized conditions, the degradation efficiency was 97.5% for MB, 80% for RhB and 85% for MO in the presence of H_2O_2 and over CdS NRs/LFO nanocomposite. The photocatalytic activity of CdS NRs/LFO was almost 16 and 8 times as high as those of the pristine CdS NRs and pure LFO, respectively. The photocatalytic activity was enhanced mainly due to the high efficiency in separation of electron–hole pairs induced by the remarkable synergistic effects of CdS and LFO semiconductors. After the photocatalytic reaction, the nanocomposite can be easily separated from the reaction solution and reused several times without loss of its photocatalytic activity. Trapping experiments indicated that ·OH radicals were the main reactive species for dye degradation in the present photocatalytic system. On the basis of the experimental results and estimated energy band positions, the mechanism for the enhanced photocatalytic activity was proposed.

Received 6th June 2019
Accepted 1st August 2019

DOI: 10.1039/c9ra04265b

rsc.li/rsc-advances

1. Introduction

In the past decades, novel visible-light-driven semiconductors have attracted considerable attention as the most promising materials in the photocatalytic field, especially for the application in degradation of organic contaminants and the conversion of solar energy.[1–4] Among various semiconducting materials, TiO_2 is probably the most promising one because of its high photocatalytic efficiency, excellent chemical and photochemical stability, environmental friendliness, and low-cost for large-scale water treatment.[5,6] However, TiO_2 can absorb only UV light in the solar spectrum, accounting for only 4–5% of sunlight, because of its large energy band gap of 3.2 eV, so that the effective utilization of visible light or solar energy is limited.[7–12] To increase the utilization efficiency of sunlight and improve the photocatalytic activity, novel visible-light photocatalysts with high activity and stability must be developed.[13–18]

Among visible-light-driven photocatalysts, cadmium sulfide (CdS), an n-type semiconductor with a band gap of ~2.4 eV, is one of the most important semiconductors and has been extensively studied during the past decades.[19–21] The narrower band gap promotes the utilization of visible light and makes CdS a competitive candidate as a visible light photocatalyst. However, the rapid recombination of the excited electron–hole pairs, low quantum yield and high susceptible to sulfide photocorrosion of the CdS-based photocatalyst are obstacles which seriously limit its further utilization in practical wastewater remediation.[22] The construction of p–n-type heterojunction composites should be a suitable strategy to delay the electron–hole pair recombination, stabilize the structure, and improve the photocatalytic activity of semiconductors.[23–27] In this context, the CdS-based heterojunctions such as CdS–TiO_2,[28] CdS–GO,[29] CdS–Bi_2MoO_6,[30] CdS–Bi_2WO_6,[31] CdS–C_3N_4 [32] and CdS–$Bi_2O_2CO_3$ [33] have been reported, which exhibited high photocatalytic activity and stability. However, the wide band gap semiconductors can not absorb as much visible light or solar energy. If CdS combines with a narrow band gap semiconductor, the light absorbing would be enhanced. Thus, the continuous development

Department of Chemistry, Lorestan University, Khorramabad, 68151-44316, Iran. E-mail: farhadi.s@lu.ac.ir; sfarhadi1348@yahoo.com; Fax: +986633120618; Tel: +986633120611

of visible light driven semiconductor cocatalysts is essential to enhance the photocatalytic activity of CdS photocatalysts.[34–37]

Perovskite-type lanthanum-orthoferrite ($LaFeO_3$) is an important p-type semiconductor which can be driven by visible light owing to the narrow band gap of ~2.0 eV.[38] $LaFeO_3$ exhibits high photocatalytic activity towards degradation of organic contaminant under visible light irradiation and it is stable in various environments.[39] Until now, a few of $LaFeO_3$-based heterojunctions such as $LaFeO_3$/Ag_3PO_4,[40] $LaFeO_3$/$SrTiO_3$,[41] $LaFeO_3$/TiO_2,[42] $LaFeO_3$/C_3N_4,[43] $LaFeO_3$/GrO,[44] $LaFeO_3$/$H_3PW_{12}O_{40}$ [45] and $LaFeO_3$/Ag_2CO_3 [46] have been reported for specific photocatalytic reactions, indicating that $LaFeO_3$-based catalysts exhibit enhanced photocatalytic activity. Therefore, the combination of n-type CdS with p-type $LaFeO_3$ semiconductor could be a good method to improve the visible light absorption capability and further enhance the photocatalytic performance of CdS under visible light irradiation. As far as we know, the combination of p-type $LaFeO_3$ and n-type CdS for photocatalytic purposes has not been reported previously.

In this work, a novel CdS nanorods/$LaFeO_3$ (CdS NRs/LFO) nanocomposite was prepared *via* a facile solvothermal method. Several spectroscopic techniques were used to characterize the CdS NRs/LFO nanohybrid. The photocatalytic performance of the CdS NRs/LFO nanocomposite for H_2O_2-assisted degradation of organic dyes such as methylene blue (MB), rhodamine B (RhB), and methyl orange (MO) under visible light irradiation has been evaluated. The effects of different parameters *i.e.*, H_2O_2 amount, catalyst dosage and initial dye concentration on the process efficiency were investigated. Furthermore, the activity of CdS NRs/LFO nanocomposite was compared with those of pure CdS NRs and LFO under similar conditions. To the best of our knowledge, there are no reports on the enhanced visible-light activities of CdS NRs for photocatalytic degradation of organic dyes by coupling with a perovskite-type mixed oxide such as LFO nanoparticles. On the basis of the calculated energy band positions and the active species during photocatalytic process, a mechanism of the photocatalysis was proposed and discussed.

2. Experimental

2.1. Materials

All reagents were purchased from Merck chemical company and used without further purification: cadmium nitrate ($Cd(NO_3)_2 \cdot 4H_2O$, 97%), thiourea (CH_4N_2S, 98.5%), ethylenediamine ($C_2H_8N_2$, 100%), potassium hexacyanoferrate(III) ($K_3[Fe(CN)_6] \cdot 5H_2O$, 99%), lanthanum(III) nitrate hexahydrate ($La(NO_3)_3 \cdot 6H_2O$, 98%), methylene blue (MB, $C_{16}H_{18}ClN_3S$, 98%), rhodamine B (RhB, $C_{28}H_{31}ClN_2O_3$, 98%), methyl orang ($C_{14}H_{14}N_3NaO_3S$, MO, 98%). All other reagents used in this study were analytically pure and used without further purification.

2.2. Characterization techniques

X-ray powder diffraction (XRD) patterns were obtained at room temperature by a XPertPro Panalytical diffractometer using Ni-filtered Cu Kα radiation (l = 1.5406 Å). Infrared spectra were obtained using a Shimadzu 160 Fourier-transform infrared spectroscopy (FTIR) instrument in the range of 4000–500 cm^{-1}. UV-Vis diffuse reflectance spectra (DRS) of photocatalyst samples were measured on Scinco S4100 spectrophotometer using $BaSO_4$ as the reference. The morphological observation and the elemental mappings were carried out with a field emission scanning electron microscopy (FESEM, Mira3 Tescan, Czech) equipped with a link energy-dispersive X-ray analyzer. Transmission electron microscopy (TEM) and high-resolution-TEM (HRTEM) images were taken on EM10C electron microscope operating at a voltage of 100 kV. The Brunauer–Emmett–Teller (BET) analysis was performed to obtain the specific surface area and porosity of samples by a PHS-1020 PHSCHINA nitrogen adsorption apparatus at 77 K. All the samples were degassed at 180 °C prior to nitrogen adsorption measurements. An adsorption isotherm was used to determine the pore size distribution by the Barrett–Joyner–Halenda (BJH) method. Magnetic measurements were employed using a vibrating sample magnetometer (VSM, Daneshpajoh Kashan Co, Iran) with a maximum magnetic field of ±10 kOe at room temperature. X-Ray photoelectron spectroscopy (XPS) measurements were obtained using the Bestec XPS system with an Mg-Kα source and photon energy of 1486.6 eV. All the binding energies were referenced to the C 1s peak at 284.6 eV of the surface adventitious carbon. The photoluminescence (PL) spectra of photocatalysts were measured using a fluorescence spectrophotometer (F-4500, Hitachi) at an excitation wavelength of 330 nm. Ultraviolet-visible (UV-Vis) spectra of dye solutions during photocatalytic degradations were recorded at room temperature on a Varian Cary 100 spectrophotometer. The content of LFO in the nanocomposite was determined by inductively coupled plasma atomic emission spectroscopy (ICP-AES, model OEC-730).

2.3. Synthesis of CdS nanorods (CdS NRs)

$Cd(NO_3)_2 \cdot 4H_2O$ (1.92 g) and thiourea (1.42 g) were added to 40 mL of ethylenediamine solvent and stirred for 15 min at room temperature. Then, the mixture was transferred into a 50 mL Teflon-lined autoclave and maintained at 180 °C for 24 h. The yellow colored precipitate was separated, washed several times with ethanol and distilled water and then dried at 80 °C for 12 h.

2.4. Synthesis of $LaFeO_3$ nanoparticles (LFO NPs)

Initially, $La[Fe(CN)_6] \cdot 5H_2O$ complex was synthesized as a reddish-brown precipitate *via* mixing aqueous solutions of equimolar amounts of $La(NO_3)_3 \cdot 6H_2O$ (2.16 g, 5 mmol) and $K_3[Fe(CN)_6]$ (1.64 g, 5 mmol) with continuous stirring, according to the literature method.[47] The resulting precipitate was washed with water, ethanol and diethyl ether, before drying in air at 50 °C. In order to prepare LFO nanoparticles, an appropriate amount (5 g) of the La $[Fe(CN)_6] \cdot 5H_2O$ complex was placed in a porcelain crucible and then heated in a furnace electric at 700 °C under air atmosphere for 2 h.

2.5. Synthesis of CdS nanorods/$LaFeO_3$ (CdS NRs/LFO)

The synthetic route to CdS NRs/LFO composite is described as follows: LFO NPs (0.1 g) were dispersed in ethylenediamine (40

mL) and sonication for 1 h. Then, $Cd(NO_3)_2 \cdot 4H_2O$ (0.32 g) and thiourea (0.16 g) were added, and the mixture was sonicated for 30 min. Then, the above mixture was transferred into a 50 mL Teflon-lined autoclave and maintained at 200 °C for 24 h. The pale green precipitate was filtered and washed several times with ethanol and distilled water and then dried at 80 °C for 12 h. For comparison, pure CdS nanorods sample was also prepared in ethylenediamine solvent under the same conditions without adding $LaFeO_3$. The ICP-AES results indicated that the loading amount of $LaFeO_3$ in the as-prepared CdS nanorods/$LaFeO_3$ (CdS NRs/LFO) nanocomposite was estimated to be 38.85 wt%.

2.6. Photocatalytic degradation of organic dyes

Visible light photocatalytic activity of the CdS NRs/LFO nanocomposite was evaluated for the degradation of MB, RhB and MO dyes in aqueous solutions. A 400 W Hg lamp with a UV cutoff filter ($\lambda > 420$ nm) was used as the visible light source. The reactions were conducted in an open Pyrex cylindrical glass vessel containing dye solution (100 mL, 25 mg L^{-1}), H_2O_2 (4 mM) and CdS NRs/LFO photocatalyst (50 mg). The suspension was magnetically stirred in the dark for 3 h to attain adsorption–desorption equilibrium prior to irradiation by visible light. At a defined time interval, 2 mL aliquots of the reaction solution were sampled, the samples were centrifuged to remove the suspended CdS NRs/LFO. The residual MB, RhB, and MO concentrations were determined on a UV-Vis spectrometer at maximum absorbance wavelengths of 664, 554, and 463 nm, respectively. The degradation percentage was calculated using: $[(C_0 - C_t)/C_0] \times 100\%$, where C_0 is the dye concentration after adsorption equilibrium and before irradiation and C is the dye concentration after irradiation.

The effects of various parameters, such as the concentration of H_2O_2 (0–5 mM), photocatalyst dosage (0–75 mg) and initial dye concentration (25–45 mg L^{-1}) were studied on the photocatalytic activity of the CdS NRs/LFO nanocomposite by a similar process described above. Photocatalytic activities of pure CdS NRs and pristine LFO were also evaluated by the degradation of MB aqueous solution in a same manner. To investigate the photocatalytic stability and reusability of the sample, the photocatalytic activity measurements mentioned above were repeated for five cycles using an aqueous MB solution (50 mL, 25 mg L^{-1}). After each cycle, the spent photocatalyst was separated from the treated MB solution, washed with deionized water, dried in an oven, and used for the next cycle.

3. Results and discussion

3.1. Characterization of the photocatalyst

Crystal structure and phase composition of the samples were first characterized by XRD and the results are shown in Fig. 1. Fig. 1(a) illustrates the XRD pattern of pure LFO nanoparticles and all peaks can be well-indexed to the perovskite-type LFO phase according to the JCPDS card no. 37-1493. The XRD pattern of pristine CdS NRs in Fig. 1(b) showed the presence of hexagonal phase as can be seen from the well-resolved

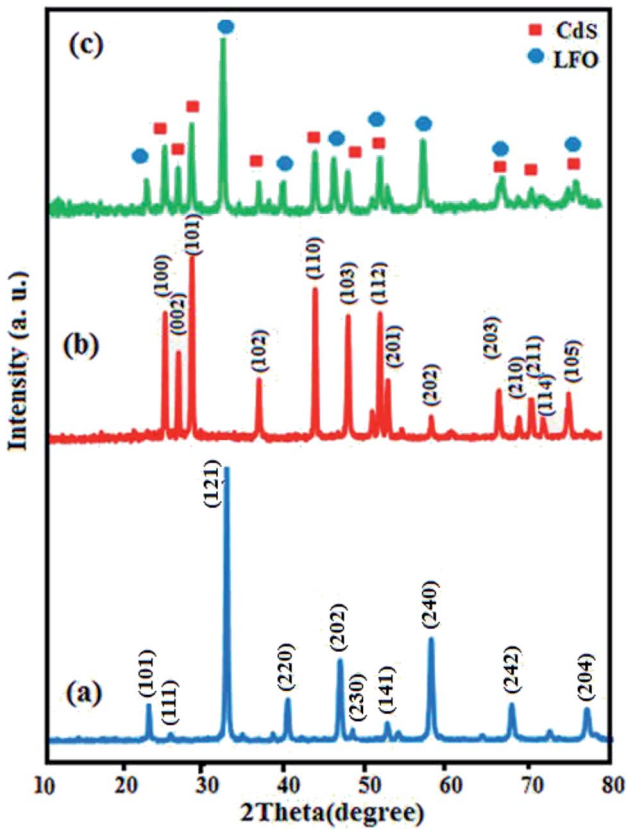

Fig. 1 XRD patterns of (a) LFO, (b) CdS NRs and (c) CdS NRs/LFO.

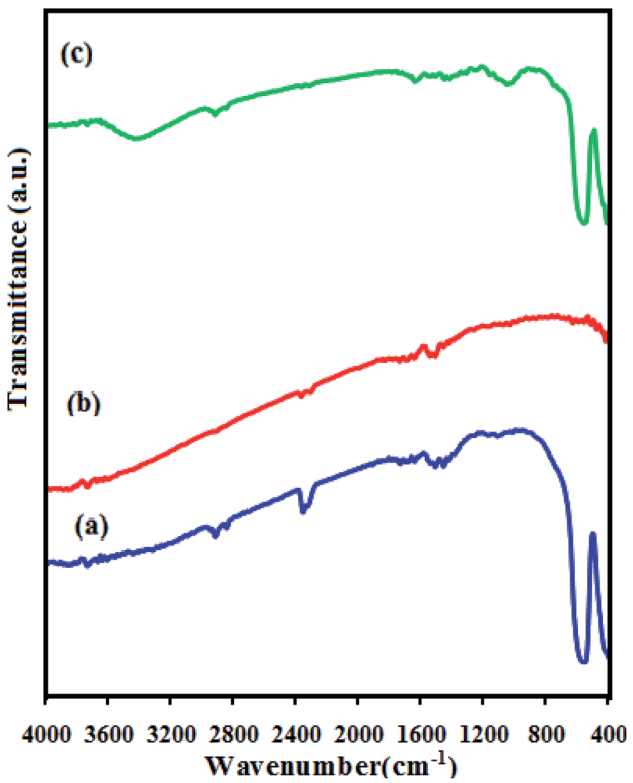

Fig. 2 FT-IR spectra of (a) LFO, (b) CdS NRs and (c) CdS NRs/LFO.

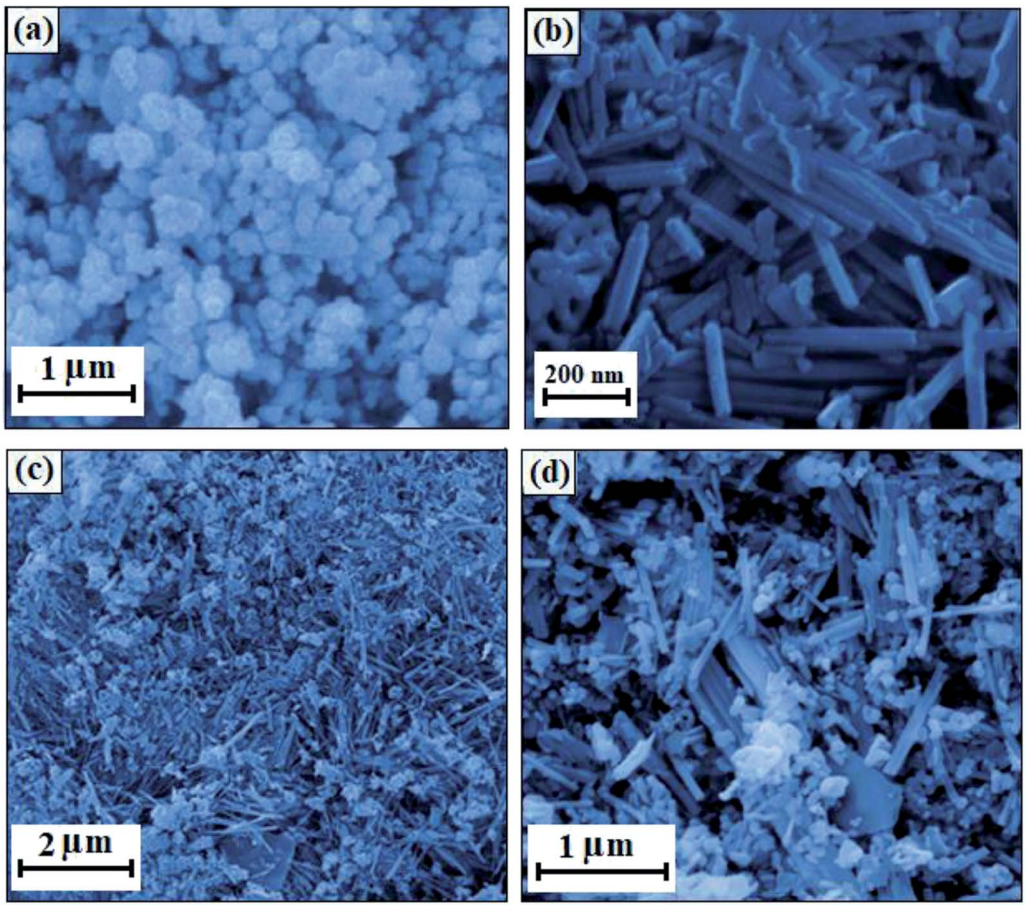

Fig. 3 SEM images of (a) LFO, (b) CdS, and (c and d) CdS NRs/LFO nanocomposite.

diffraction peaks and the excellent matching of the diffraction pattern with the database pattern (JCPDS card no. 75-1545). The diffraction pattern of the nanocomposite in Fig. 1(c) exhibited diffraction peaks corresponding to both CdS NRs and LFO and no other impure peaks can be observed, indicating that the sample is composed of LFO and CdS NRs and the CdS NRs/LFO nanocomposite has been successfully prepared. The Debye–Scherrer formula (eqn (1)) was used to calculate the crystallite size of the LFO nanoparticles:[48]

$$D_p = 0.94\lambda/(\beta_{1/2}\cos\theta) \quad (1)$$

where λ is the wavelength (Cu-Kα), $\beta_{1/2}$ is the broadening of the diffraction line measured at half of the maximum intensity, θ is the Bragg angle for a given diffraction, and D_p represents the crystallite size. The crystallite size of the LFO nanoparticles was found to be 85 nm from the highest intensity peak of the (121) plane.

FT-IR spectra of the as-prepared CdS NRs, LFO, and CdS NRs/LFO nanocomposite are indicated in Fig. 2. In the spectrum of LFO in Fig. 2(a), the strong bands at about 557 and 430 cm^{-1} are assigned to the Fe–O stretching and bending vibrations of the octahedral FeO_6 groups in the perovskite-type structure, respectively.[49] The FT-IR spectrum of the CdS in Fig. 2(b) does not show any band due to the Cd–S vibration appears below 400 cm^{-1}.[50] Fig. 2(c) shows the FT-IR spectrum of the CdS NRs/LFO nanohybrid, which displayed two main absorption bands below 1000 cm^{-1}. These bands could be related to the LFO nanoparticles in the nanocomposite. It is noted that in some spectra broad bands appeared at about 3550 and 1600 cm^{-1} which are related to the stretching and bending vibrations of the water molecules absorbed by the sample or KBr pellet. Also, in the FT-IR spectra of samples weak bands were observed in the 2400 cm^{-1} which are attributable to atmospheric CO_2 gas chemisorbed on the surface of the samples particles during handling to record the spectra.

The morphology and microstructure of the CdS NRs/LFO nanocomposite were investigated by scanning electron microscopy (SEM). As shown in Fig. 3, the SEM images of LFO nanoparticle and CdS NRs nanohybrid reveal spherical and nanorod morphologies respectively. The image in Fig. 3(a) indicates that the synthesized LFO nanoparticles are about 80 nm in diameter size. SEM image in Fig. 3(b) show that the CdS NRs have a rough surface and porous structure, and are about 50–80 nm in diameter and 2–3 μm in length which could be used for further to make the LFO spheres on the surface. During the of CdS NRs/LFO hybrid formation, LFO spheres with an average size of 80 nm were formed on the surface of CdS NRs as shown in Fig. 3(c) and (d), confirming the decoration of

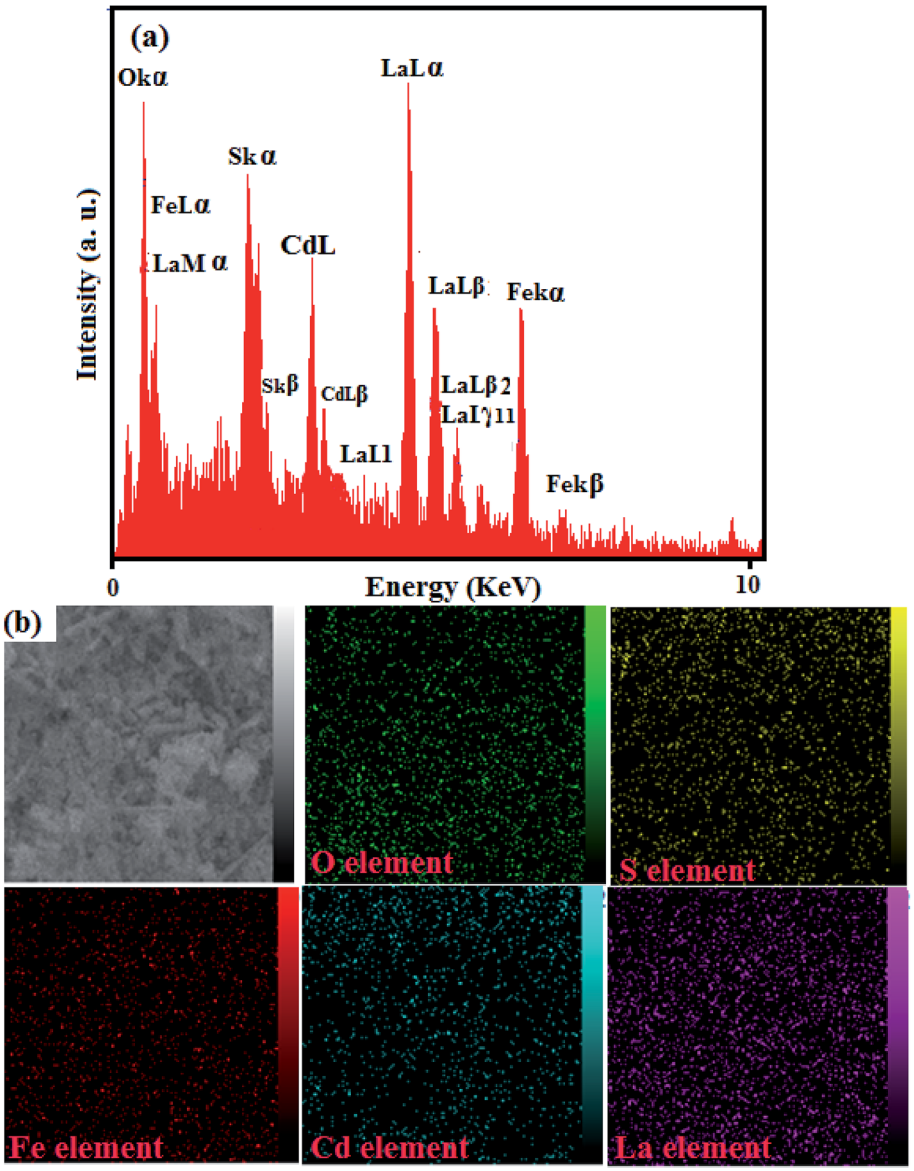

Fig. 4 (a) EDX spectrum and (b) EDX mappings of the CdS NRs/LFO nanocomposite.

LFO NPs on the surfaces of the CdS nanorods. Indeed, the CdS NRs in CdS NRs/LFO are rougher than those of pure CdS NRs, because the LFO nanoparticles cover the surface of CdS NRs.

The existence of elements in the CdS NRs/LFO nanocomposite and its chemical composition was further confirmed by EDX spectroscopy and the results are shown in Fig. 4. The EDX spectrum of the nanocomposite in Fig. 4(a) shows the peaks of Cd, S, La, Fe, and O elements at their corresponding keV values. The distribution of elements present in the nanocomposite was studied using SEM-EDX mapping analysis as shown in Fig. 4(b). The elemental mappings show La, Fe, Cd, S and O elements were uniformly distributed over the nanocomposite, confirming the homogeneity of the sample.

TEM and HRTEM images of the heterogeneous CdS nanoparticles/LFO sample are shown in Fig. 5. As shown in Fig. 5(a) and (b), sphere-like LFO nanoparticles with sizes of about 70–85 nm were evenly dispersed and embedded on the external surface of CdS NRs with diameters of 50–80 nm. It is clearly shown that the LFO nanoparticles partly cover the surface of CdS NRs, which is consistent with the SEM observation. The coexistence of CdS and LFO can be confirmed by high-resolution TEM (HRTEM) image. The local HRTEM image of the CdS NRs/LFO (marked in Fig. 5(b)) is shown in Fig. 5(c). The inter-layer distance of 0.34 nm estimated in the nanorod domain was in good agreement with the *d*-spacing of the (002) planes of the hexagonal CdS, whereas the inter-layer distance of 0.39 nm identified in the nanoparticle domain was in good agreement with the *d*-spacing of the (101) planes of the perovskite-type LFO, together indicating that LFO NPs were tightly attached to the CdS surface. These results confirm

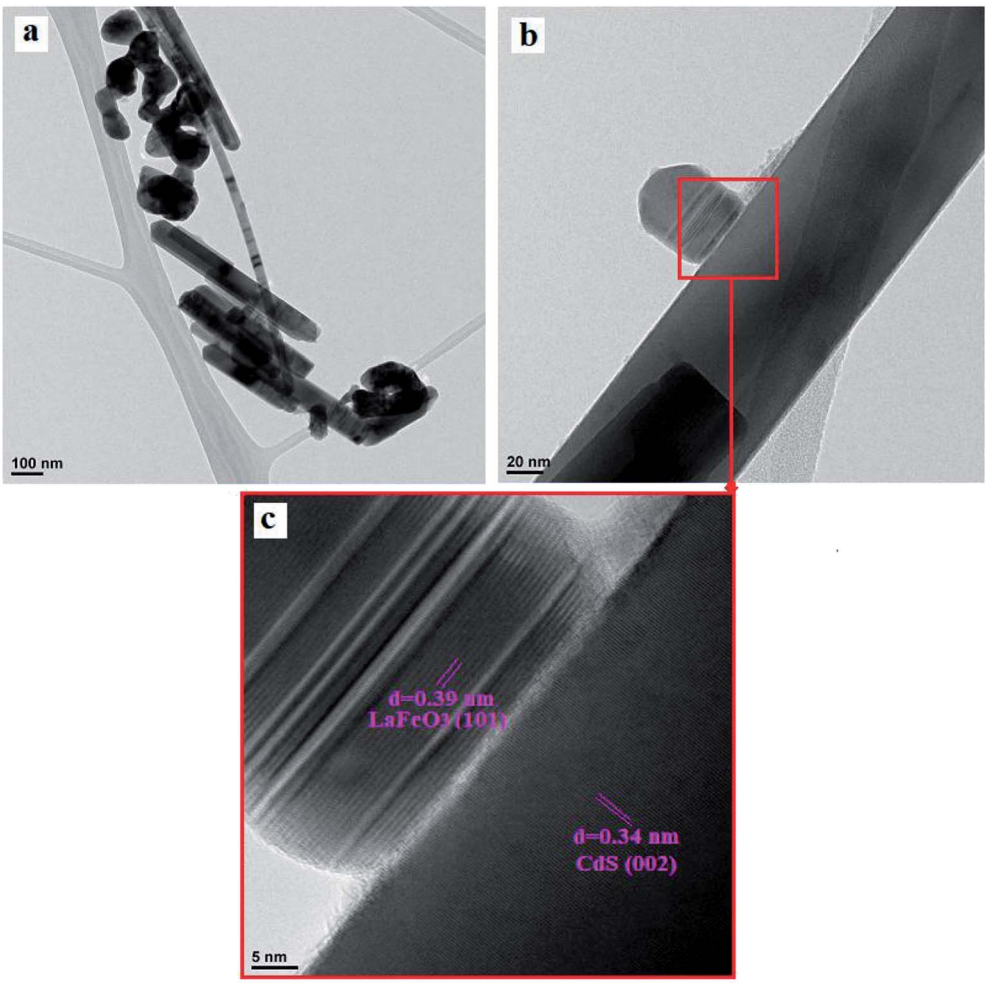

Fig. 5 (a and b) TEM images and (c) HR-TEM image of the CdS NRs/LFO nanocomposite.

that a CdS NRs/LFO heterojunction is well-constructed between CdS NRs and LFO nanoparticles. This heterojunction between n-type CdS and p-type LFO can facilitate the charge transfer more readily to significantly reduce the recombination of electron–hole pairs as well as to enhance the visible-light-driven photocatalytic activity of CdS NRs/LFO nanocomposite.

The optical properties of as-synthesized CdS NRs, LFO and CdS NRs/LFO samples were investigated by UV-Vis DRS absorption spectroscopy as shown in Fig. 6. According to the spectrum in Fig. 6(a), the CdS sample exhibited strong absorption in the $\lambda <$ 540 nm region.[51] However, after coupling CdS with LFO, the obtained composite exhibited a wider absorption band in the visible region. The CdS NRs/LFO composite sample was red shifted compared with CdS. This was attributed to LFO particles assembled on the surface of CdS NRs acting as a visible light semiconductor to extend the optical response. Obviously, the visible light absorption of CdS NRs/LFO heterojunction is better than that of CdS, which possibly results good visible-light utilization. The band gap energy (E_g) of samples can be deducted from the formula:[51,52] $(\alpha h\nu)^2 = B(h\nu - E_g)$, where α, ν, and B are absorption coefficient, light frequency and proportionality constant, respectively. The $(\alpha h\nu)^2$ *versus* $h\nu$ curves for CdS NRs, LFO and CdS NRs/LFO nanocomposite are shown in Fig. 6(b)–(d). The value of $h\nu$ extrapolated to $\alpha = 0$ gives the absorption band gap energy. The band gap energies were estimated to be 2.4, 2.2 and 2.3 eV for CdS NRs, LFO and CdS NRs/LFO nanocomposite samples, respectively, indicating that the introduction of LFO decreased the E_g of CdS. Furthermore, the decrease of E_g upon composite formation confirms electronic coupling between CdS and LFO. The visible light photocatalytic activity of CdS NRs/LFO nanocomposite could be attributed to the existence of this broad band with the E_g of 2.3 eV.

The magnetic behaviors of the pure LFO NPs and CdS NRs/LFO nanocomposite were analyzed by VSM at room temperature. The coercive force (H_c), saturation magnetisation (M_s), and remanent magnetisation (M_r) of CdS NRs/LFO were compared with those of LFO nanoparticles in the inset of Fig. 7. The LFO nanoparticle showed weak magnetic properties with saturation magnetization about 0.31 emu g^{-1}. After decoration of LFO nanoparticles on the surfaces of the CdS NRs, the M_s decreases obviously. Because of the diamagnetic property of CdS, the saturation magnetization of CdS NRs/LFO composite is reduced to 0.18 emu g^{-1} as compared with that of pure LFO (0.31 emu g^{-1}). This result further indicates that the LFO nanoparticles have been successfully loaded on the surface of CdS NRs.

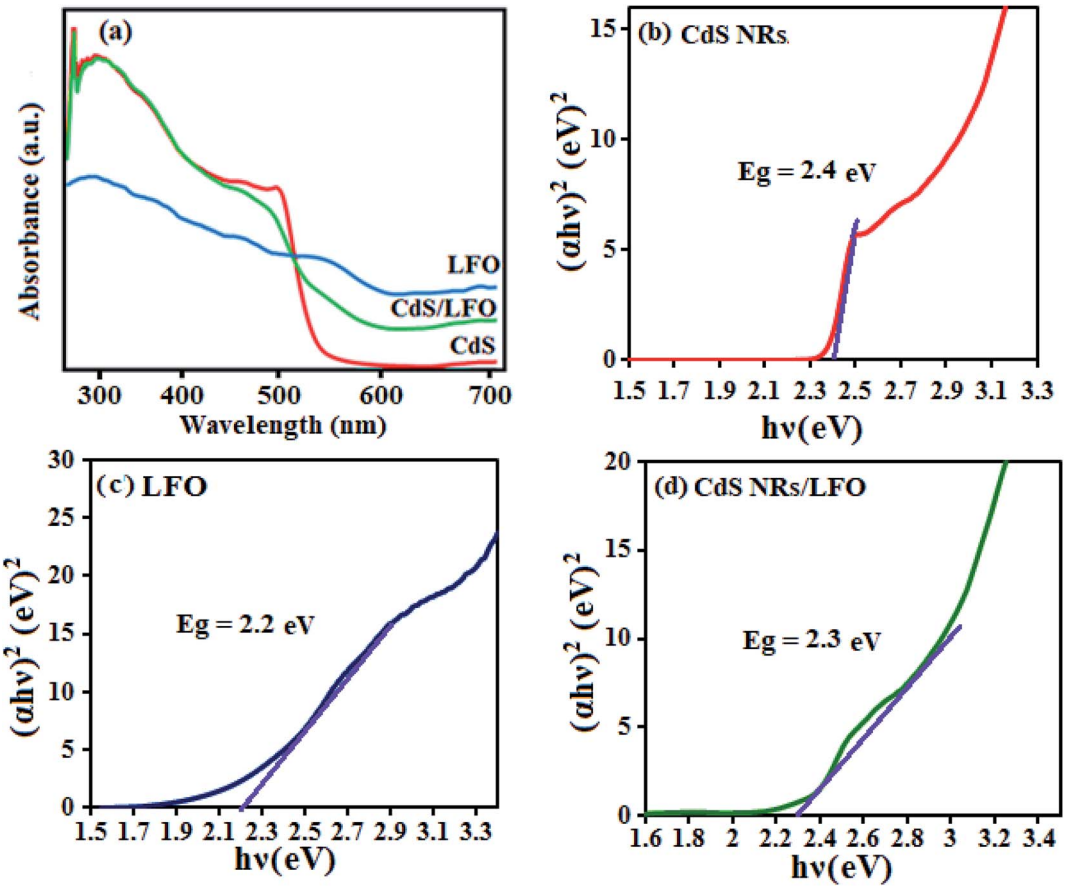

Fig. 6 (a) UV-Vis diffuse reflectance spectra and (b–d) band gap energies of different photocatalyst samples.

The porosity and specific surface area of pristine CdS NRs, pure LFO and CdS NRs/LFO nanocomposite samples were investigated through nitrogen adsorption–desorption isotherms and the results are shown in Fig. 8. Based on the IUPAC definition, these isotherms can be classified to type-IV, suggesting the presence of porous structures. Nevertheless, the samples indicate different hysteresis loops. The pure CdS

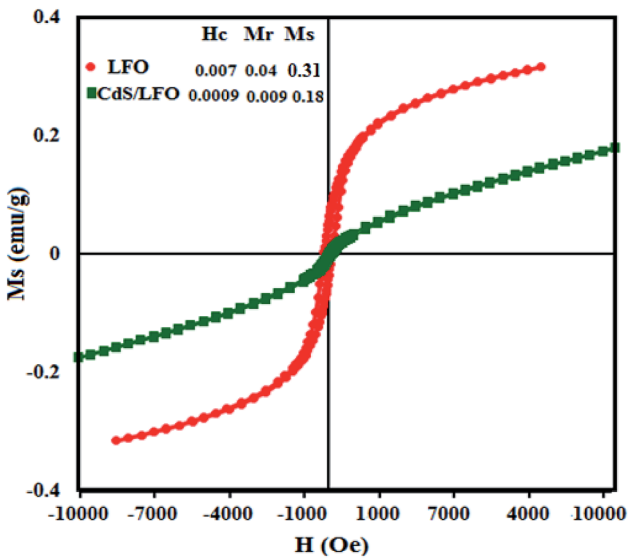

Fig. 7 Room-temperature magnetization (MS) curves of LFO and CdS NRs/LFO.

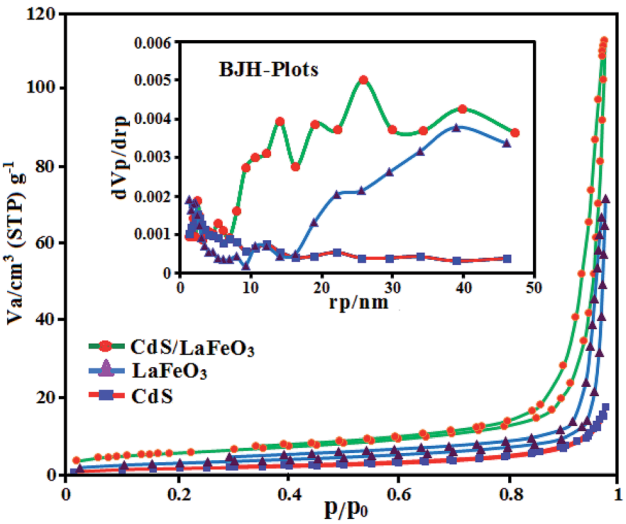

Fig. 8 N_2 adsorption–desorption isotherms of CdS NRs, LFO and CdS NRs/LFO samples. The inset show the corresponding BJH pore size distribution curves.

Table 1 The textural properties of as-prepared samples

Sample	BET surface area (S_{BET}, $m^2\ g^{-1}$)	Total pore volume (V_p, $cm^3\ g^{-1}$)	Average pore diameter (r_p, nm)
CdS	5.02	0.0262	21.46
$LaFeO_3$	10.23	0.1111	43.44
CdS/$LaFeO_3$	18.28	0.1719	38.25

NRs exhibits a very small hysteresis loops. The hysteresis loops of the as-prepared LFO and CdS NRs/LFO samples are of type H3 in the range of $p/p_0 = 0.7$–1.0 and the saturated adsorption state cannot be achieved till $p/p_0 = 1.0$. This clearly suggests the formation of mesopores and macropores in the above materials and is in good agreement with their corresponding pore size distributions in the inset of Fig. 8. The Brunauer–Emmett–Teller (BET) surface area, the pore volume and average pore size for CdS NRs, LFO and CdS NRs/LFO were calculated and the results are presented Table 1. As given in Table 1, the pore volume and average pore size of the CdS NRs/LFO composite material were found to be higher than pure CdS NRs. Furthermore, the BET surface area of composite is relatively high (18.28 $m^2\ g^{-1}$) compared to that of pure CdS NRs (5.02 $m^2\ g^{-1}$). This could be related to decrease stacking and impeded aggregation of CdS NRs due to the presence of LFO nanoparticles. LFO nanoparticles could not only prevent agglomeration of the CdS NRs and enable a good dispersion of these rod-like particles, but also substantially enhance the porosity and specific surface area of the composite. It can be concluded that introduction of LFO nanoparticles has a good effect on the structure of CdS NRs and increases the surface area and porosity of CdS NRs which are all useful factors for improving the adsorption and photocatalytic performance (indicated later).

The surface composition and chemical state of atoms in the CdS NRs/LFO composite were further analyzed by X-ray photoelectron spectroscopy (XPS). The survey spectrum in Fig. 9(a) indicates the coexistence of Cd, S, La, Fe, and O elements in the composite and no other element signals can be detected, suggesting the high purity of the composite. Fig. 9(b) displays the XPS spectrum of S 2p region, which contains two peaks at 161.95 eV and 162.71 eV assigned to S $2p_{3/2}$ and S $2p_{1/2}$, respectively, implying that the sulfur occurred as S^{2-} ions.[53] The high resolution XPS spectrum of Cd 3d in Fig. 9(c) shows two peaks at 405.58 eV and 412.32 eV which were belong to Cd $3d_{5/2}$ and Cd $3d_{3/2}$ energy levels respectively.[54] The spin orbit separation of the 3d orbital is 6.74 eV, demonstrating that the Cd element in samples exists in the state of Cd^{2+} ions.[55] For pure CdS (XPS not shown here), the Cd $3d_{5/2}$ and $3d_{3/2}$ peaks are located at 403.70 eV and 410.50 eV, respectively. After coupling with LFO, a positive shift of 2 eV is obviously seen in comparison with pure CdS. The result is attributed to the electron transfer from CdS to LFO. Such a transfer is very favorable to improve the performance of catalyst. In Fig. 9(c), the peaks of Fe $2p_{3/2}$ and Fe $2p_{1/2}$ at 711.35 and 725.69 eV, respectively, were assigned to the core level spectra of Fe^{3+} in its oxide form.[56] Two La 3d peaks at 836.06 and 852.30 eV in Fig. 9(d) were identified as spin–orbit splitting of $3d_{5/2}$ and $3d_{3/2}$ of La^{3+}, respectively, in the oxide.[57] The O 1s peaks (not shown here) can be deconvoluted into three peaks, corresponding to the surface adsorbed oxygen species, the oxygen of surface hydroxyl and the perovskite lattice oxygen of LFO. The XPS results further confirm the formation of CdS NRs/LFO composite, especially, the presence of strong interaction between CdS and LFO, consistent with the XRD and HR-TEM. In particular, compared with the Cd 3d and S 2p peaks in the spectrum of pure CdS (XPS not shown here), those in the spectrum of CdS NRs/LFO composite are shifted to higher binding energies. Such a shift reflects the decrease in electron density around both Cd^{2+} and S^{2-} due to electron transfer from CdS to LFO in the CdS NRs/LFO structure, which is very favorable to improve the performance of photocatalyst.

3.2. Photocatalytic degradation of dyes

The photocatalytic performance of CdS NRs/LFO nanocomposite was investigated for degradation of organic dyes irradiated with visible light. A series of experiments were carried out to investigate the MB dye degradation under different conditions, and the results are presented in Fig. 10(a). As can be seen, the ability of photo alone or H_2O_2/photo for degrading MB was negligible. In the control experiments, no degradation of MB was observed in the absence of photocatalyst, indicating that MB was stable and did not undergo a photolytic process. The degradation efficiency of MB by H_2O_2 and in the absence of catalyst was about 4% within 180 min of irradiation, which can be attributed to slight production of hydroxyl radicals through direct photo decomposition of H_2O_2. Furthermore, the degradation efficiencies of MB with the CdS NRs/H_2O_2/photo, CdS NRs/LFO/H_2O_2/(in dark), LFO/H_2O_2/photo, and CdS NRs/LFO/photo systems were 23%, 26%, 33%, and 46%, respectively. It is noted that the MB dye is degraded by CdS NRs/LFO/H_2O_2 system in dark and the initial absorbance decreased about 26% under this condition. This weak degradation had occurred after maintaining the suspension in the dark for 3 h to establish an adsorption–desorption equilibrium when H_2O_2 was present. It is interesting to note that some perovskite-type Fe-based materials have been confirmed as heterogeneous Fenton-like catalysts.[57–59] Then, perovskite-type $LaFeO_3$ (LFO) in the CdS NRs/LFO is probably acting as heterogeneous Fenton-like catalyst. When H_2O_2 was introduced into the reaction suspension, the interfacial Fe atoms of LFO nanoparticles (denoted as Fe^{III}) could react with H_2O_2 to form ·OH radicals through Fenton-like reaction, leading to the degradation of organic dyes in dark.[60] The main Fenton-like process in dark could be depicted as below (eqn (2)–(4)):

$$Fe^{III} + H_2O_2 \rightarrow Fe^{II} + \cdot OOH + H^+ \quad (2)$$

$$Fe^{III} + \cdot OOH \rightarrow Fe^{II} + O_2 + H^+ \quad (3)$$

$$Fe^{II} + H_2O_2 \rightarrow Fe^{III} + \cdot OH + OH^- \quad (4)$$

However, under visible-light illumination, an obvious enhancement in the efficiency of MB degradation by CdS NRs/LFO/H_2O_2 system was observed and 97.5% of dye is degraded after 3 h. The above results confirmed that visible light, H_2O_2, and CdS NRs/LFO binary nanocomposite are essential elements

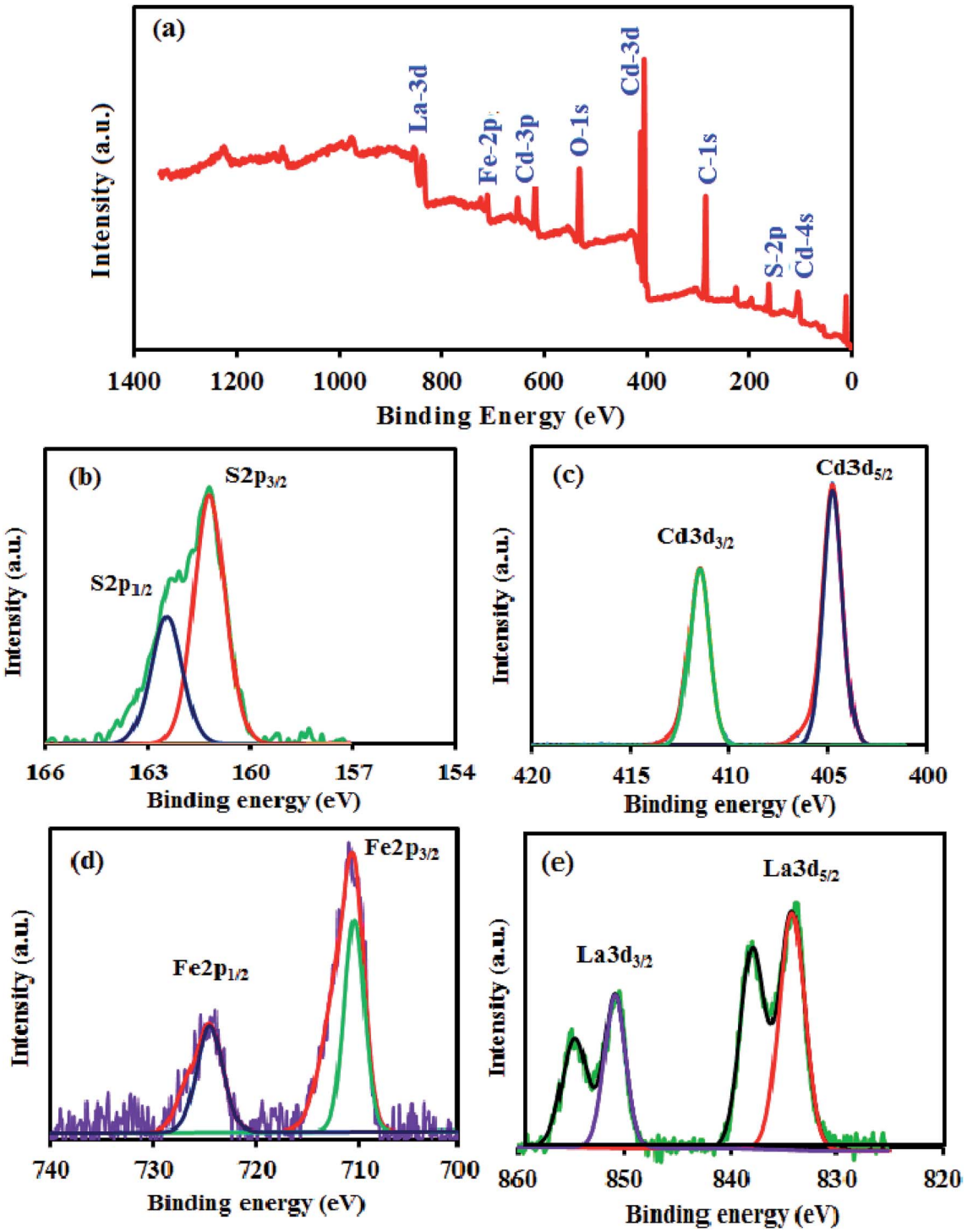

Fig. 9 XPS of the CdS NRs/LFO nanocomposite: (a) survey spectrum, (b) S 2p spectrum, (c) Cd 3d spectrum, (d) Fe 2p spectrum and (e) La 3d spectrum.

for efficient degradation of MB. Fig. 10(b) shows the change in the absorption spectrum of MB as a function of irradiation time. In the presence of photocatalyst and H_2O_2, the intensity of the characteristic absorption peak of MB at 664 nm decreased gradually with time and it approximately disappeared after 3 h. Similar behaviors were observed for the RhB and MO dyes. As shown in Fig. 10(c) and (d), the characteristic absorption peaks of RhB and MO at 554 nm and 463 nm, respectively, decrease as time increases.

The degradation rates (C/C_0) of dyes as a function of irradiation time are compared in Fig. 11(a). After irradiation for 180 min, the degradation percentages were 97.5% for MB, 80% for RhB, and 85%

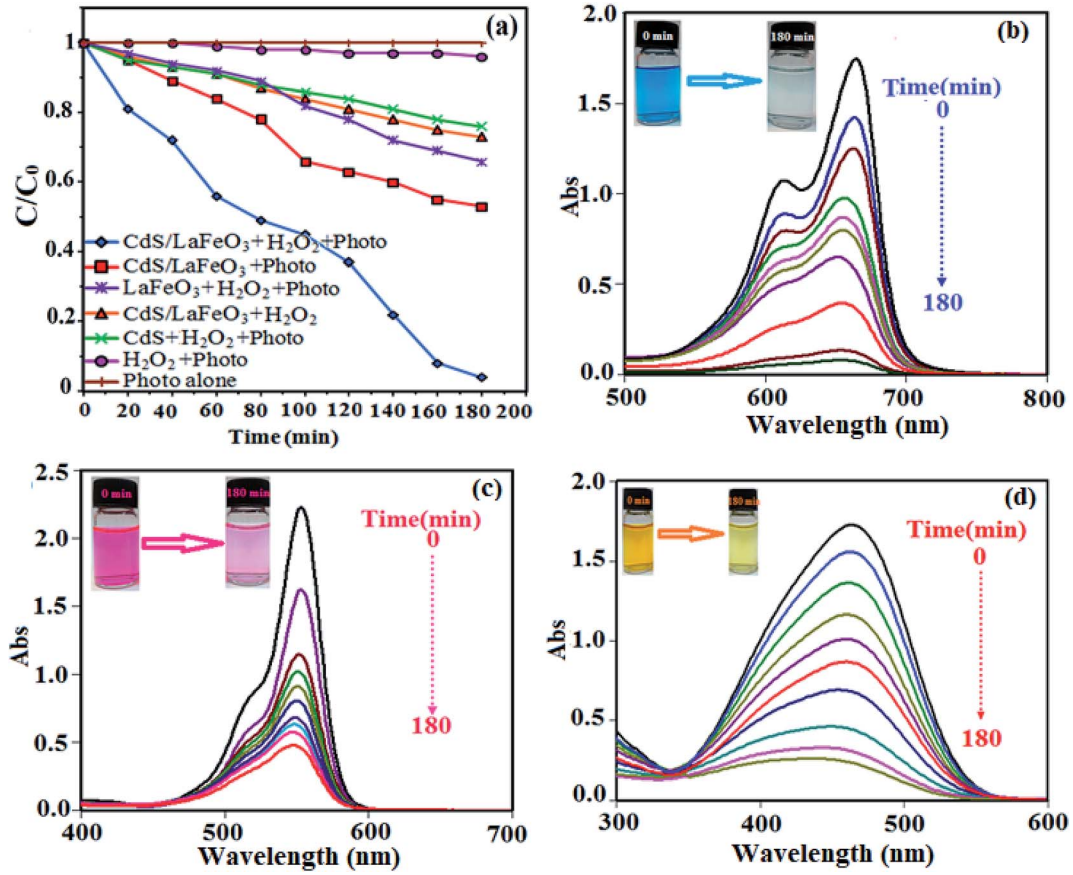

Fig. 10 (a) Photocatalytic degradation rate of MB under different conditions. Time-dependent UV-Vis spectral changes of (b) MB, (c) RhB and (d) MO solutions over CdS NRs/LFO nanocomposite and under visible irradiation. The inset photos in (b) and (c) show the color change of dyes solutions during irradiation.

for MO. The degradation kinetics of MB dye was also investigated through the rate constant (k) for a better comparison of the photocatalytic efficiency of the samples. Then, to estimate the rate of the reaction in the photodegradation experiments, the pseudo-first-order equation was used:[61] $\ln(C_0/C) = kt$, where C_0 and C are the dye concentrations before and after irradiation, respectively, k is the pseudo-first-order rate constant, and t is the reaction time. The calculated photocatalytic reaction rate constants (k) in this work are displayed in Fig. 11(b). The rate constant k in different systems increased in the order of CdS NRs/H_2O_2/photo (0.001 min^{-1}) < LFO/H_2O_2/photo (0.002 min^{-1}) < CdS NRs/LFO/photo (0.003 min^{-1}) < CdS NRs/LFO/H_2O_2/photo (0.016 min^{-1}). Among them, CdS NRs/LFO/H_2O_2/photo system represents the best catalytic performance (97.5% within 3 h) with a rate constant of 0.016 min^{-1}, which is improved by more than 16 and 8 times ($k = 0.016$ min^{-1}) compared to pure CdS ($k = 0.001$ min^{-1}) and pristine LFO ($k = 0.002$ min^{-1}), respectively. Pristine CdS and pure LFO exhibit poor photocatalytic activities, and only 46% and 33% of MB are removed within 3 h of irradiation, respectively, which result from the rapid recombination of photoexcited charges. Once CdS particles are hybridized with LFO, the photodegradation rate for the composites prominently increases.

3.2.1. Effect of H_2O_2 concentration. The effect of H_2O_2 amount on the catalytic efficiency was investigated, the dye concentration and other parameters were kept constant and the H_2O_2 concentration was varied. The results are shown in Fig. 12(a). It can be clearly seen that, in the absence of H_2O_2, only 46% of MB was degraded. While by increasing the amount of H_2O_2, from 0 mM to 4 mM the degradation efficiency increased correspondingly from 46 to 97.5%. This degradation rate enhancement was attributed to an increase in ·OH as a result of the higher H_2O_2 dosage. However, more increasing the H_2O_2 amount to 5 mM, the degradation efficiency decreases. The excess H_2O_2 molecules act as a scavenger of ·OH to generate perhydroxyl (·OOH) radicals with lower oxidation potential.[62]

3.2.2. Effect of catalyst dosage. Fig. 12(b) shows the effect of CdS NRs/LFO dosage on the photocatalytic degradation of MB in solutions containing the initial dosage range of 0–75 mg nanocomposite and H_2O_2 (4 mM) under the constant irradiation time (180 min). The degradation of MB was negligible in the absence of the CdS NRs/LFO nanocomposite. The degradation rate was observed to increase with increasing catalyst dosage and an optimum degradation of 97.5% was found at a dosage of 50 mg. Further increasing the catalyst dosage past this value resulted in a decrease in catalytic efficiency. Higher dosages of photocatalyst were thought to absorb more incident photons and produce more photogenerated charges carriers and also more ·OH radicals due to more active sites, up to an

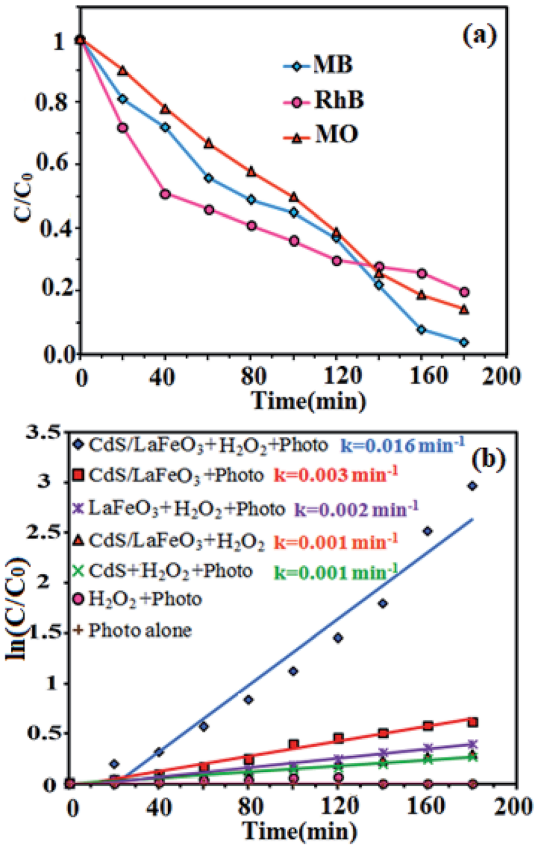

Fig. 11 (a) Comparison of the concentration changes (C/C_0) of dyes as a function of irradiation time, and (b) the degradation kinetics of MB dye under different conditions. Conditions: [dye] = 25 mg L^{-1}, 100 mL; [catalyst] = 50 mg; [H_2O_2] = 4 mM at 25 °C ± 2.

optimum value of dosage where the maximum photocatalytic activity was realized. Past this optimum, the particles suspended in the solution were thought to cause shielding and light scattering, affecting the light transmittance in solution. In addition, the photons could not be continuously injected into photocatalyst particles and may have accelerated the recombination of electrons and holes.[63] Therefore, excess catalyst dosage resulted in the decrease of the photocatalytic activity past the optimum value.

3.2.3. Effect of initial dye concentration. The effect of initial solution dye concentration on its photocatalytic degradation efficiency was investigated, as it is an important parameter in the degradation of organic pollutants. MB concentrations in the range of 25–45 mg L^{-1} were studied, and the results were shown in Fig. 12(c). The activity tended to decrease with increasing MB concentration, where the observed difference may have been due to the effect of dye concentration on the light penetration into solution.[64] The solution transmittance decreased with increasing concentration, resulting in fewer photons reaching the catalyst surface, and this was thought to have a negative influence on the separation of photogenerated charge carriers, and causing a reduction in degradation activity. This result was consistent with literature for the effect of initial concentration on photocatalysis.[65]

3.2.4. Studies of photocatalytic degradation mechanism. The position of conduction band (CB) and valence band (VB) of a semiconductor is one of the important factors that affect the photocatalytic activity. The potentials of the conduction band (CB) and valence band (VB) edges of LFO and CdS NRs were calculated according to the Mulliken electronegativity theory, which is shown as follow in eqn (5) and (6):[66]

$$E_{VB} = \chi - E_e + 0.5E_g \quad (5)$$

$$E_{CB} = E_{VB} - E_g \quad (6)$$

where E_{VB} and E_{CB} stand for the conduction band and valence band edge potential, respectively, χ is the absolute electronegativity of the semiconductor, which is the geometric mean of the electronegativities of the constituent atoms. The χ value is calculated to be 5.96 eV for CdS and 5.70 eV for $LaFeO_3$, respectively. Ee is the energy of free electrons on the hydrogen scale (4.5 eV *vs.* NHE), E_g is the band gap of semiconductor. The calculated E_{CB} = 0.03 eV, E_{VB} = 2.16 eV for LFO and E_{CB} = −0.52 eV, E_{VB} = 1.88 eV for CdS. These results confirm that CdS and LFO can form an overlapping band structure. Based on all the information presented above and literatures,[30–33,41–44] a possible mechanism of charge transfer in CdS NRs/LFO-visible light system is proposed in Fig. 13. Under visible-light irradiation, both CdS NRs and the LFO can absorb the photon energy and produce the electron–hole pairs. Since, the flat band potential of CdS is more negative than that of LFO, the electrons keep transferring from CdS to LFO until the Fermi level equilibrium of both is attained. Meanwhile, photoinduced holes from valence band (VB) of LFO would be immigrated to the less positive VB of CdS. The electrons in CB reacted with H_2O_2 to produce hydroxyl radicals (·OH), which were active enough to degrade MB. Furthermore, the VB edge potential of CdS (1.88 eV) was less positive than $E_0(\cdot OH/OH^-)$ (+2.38 eV), confirming that the photogenerated holes could not oxidize OH^- or H_2O to yield ·OH. The holes stored in the VB of CdS can also oxidize organic pollutants directly. Finally, the active species oxidize the dye molecules to the degradation products such as CO_2, H_2O, SO_4^{2-}, NO_3^-, NH_4^+ and Cl^- (eqn (7)–(9)).

$$\text{CdS NRs/LFO} + \text{visible light} \rightarrow \text{CdS NRs } (h_{VB}^+) + \text{LFO } (e_{CB}^-) \quad (7)$$

$$H_2O_2 + e_{CB}^- \rightarrow \cdot OH + OH^- \quad (8)$$

$$\text{MB dye} + \cdot OH \text{ or } h_{VB}^+ \rightarrow CO_2 + SO_4^{2-} + NO_3^- + NH_4^+ + Cl^- + H_2O \quad (9)$$

The overall degradation process of MB dye over the CdS NRs/LFO nanocomposite photocatalyst and under visible light irradiation can be written as follows (eqn (10)):

$$\text{MB dye } (C_{16}H_{18}ClN_3S) + H_2O_2 \rightarrow CO_2 + SO_4^{2-} + NO_3^- + NH_4^+ + Cl^- + H_2O \quad (10)$$

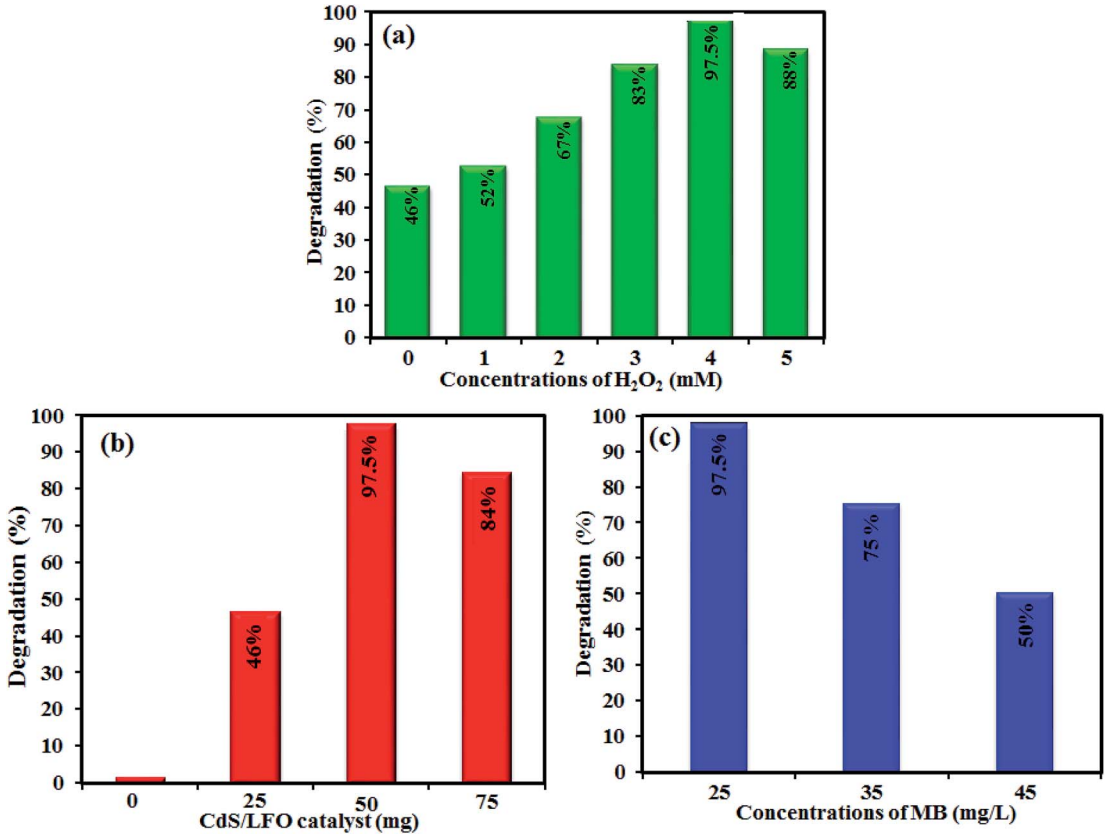

Fig. 12 The effects of (a) H_2O_2 amount, (b) photocatalyst dosage, and (c) initial dye concentration on visible-light driven photodegradation efficiency. Conditions: [MB] = 25 mg L^{-1}, 100 mL, [cat] = 50 mg, [H_2O_2] = 4 mM, 25 °C and time = 180 min.

3.2.5. Evidences of the mechanism. In order to identify the active species generated over CdS NRs/LFO heterojunction and confirm the mechanism of photocatalysis, the trapping experiments were performed.[67] Isopropyl alcohol (IPA) and disodium ethylene-diaminetetraacetate (EDTA-2Na) were used as the scavengers of the hydroxyl radical (·OH) and photogenerated holes (h^+), respectively.[68,69] By adding two different scavengers in MB solution with CdS NRs/LFO heterojunction, trapping experiments were conducted to find out the most effective species. As shown in Fig. 14(a), the MB degradation is significantly inhibited and only 36% of the dye is degraded on adding IPA as a scavenger of the hydroxyl radical (·OH) to the reaction

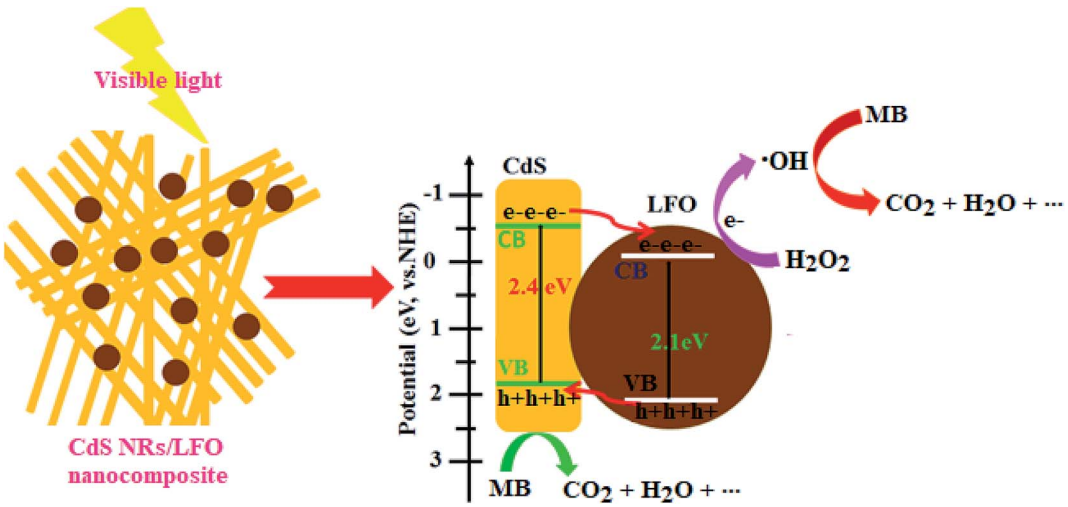

Fig. 13 Schematic diagram of the charge separation and possible photocatalytic degradation mechanism for CdS NRs/LFO heterojunction under visible light irradiation.

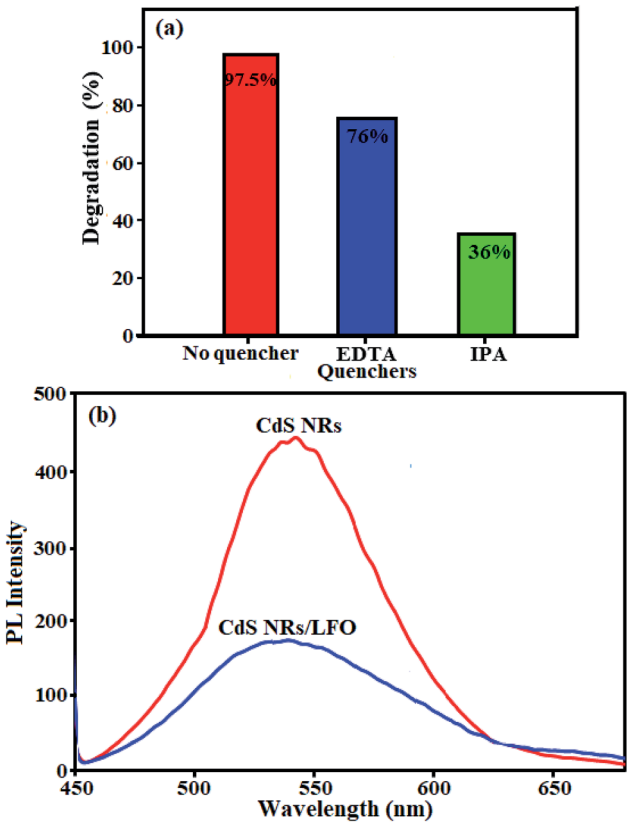

Fig. 14 (a) Quenching tests with and without quenching agents, and (b) Photoluminescence (PL) spectra of pure CdS NRs and CdS NRs/LFO nanocomposite.

solution. This implies that the dye degradation is highly correlated with ·OH and the ·OH radicals formed through the direct reaction of photogenerated electrons with the H_2O_2 molecules are the major active species responsible for MB degradation. On the contrary, the addition of EDTA-2Na as a scavenger of the holes (h^+) to the reaction solution has only a minor suppression on the degradation of MB and the dye degradation still maintains a high level of 76% after 3 h of photocatalysis, indicating that h_{VB}^+ is not the dominant reaction species in the photocatalysis. This means that the oxidation of dye molecules occurs directly by the photoinduced holes as a minor reaction.

The migration and separation efficiency of photo-generated charge carriers between the two semiconductors in the nanocomposite were extensively investigated by photoluminescence (PL) spectroscopy.[70–79] PL spectroscopy is a useful technique to survey the separation efficiency of the photogenerated electron–hole pairs in semiconductors because the electron–hole recombination's in semiconductors are mainly responsible for PL emissions.[80,81] Actually, the PL emission is a mainly consequence of the recombination of photoexcited electron–hole pairs, and a lower PL intensity indicates a lower recombination rate of photoexcited electron–hole pairs.[82–85] PL spectra are presented in Fig. 14(b) for pure CdS and the CdS NRs/LFO composite. A main emission peak was observed at about 540 nm for the pure CdS which was attributed to fast recombination of electron–hole pairs in the CdS material.[86,87] The intensity of this emission peak significantly decreased upon LFO loading, but the fluorescence emission peak position did not change. This indicated that the recombination of the photoexcited electrons and holes was greatly reduced by coupling the CdS and LFO. As we known, intensity of the PL spectrum of a semiconductor mainly results from the recombination of electrons–holes pairs. Hence, there is a strong correlation between PL emission intensity and separation of the photogenerated charge carriers.[88] For this reason, the weakened

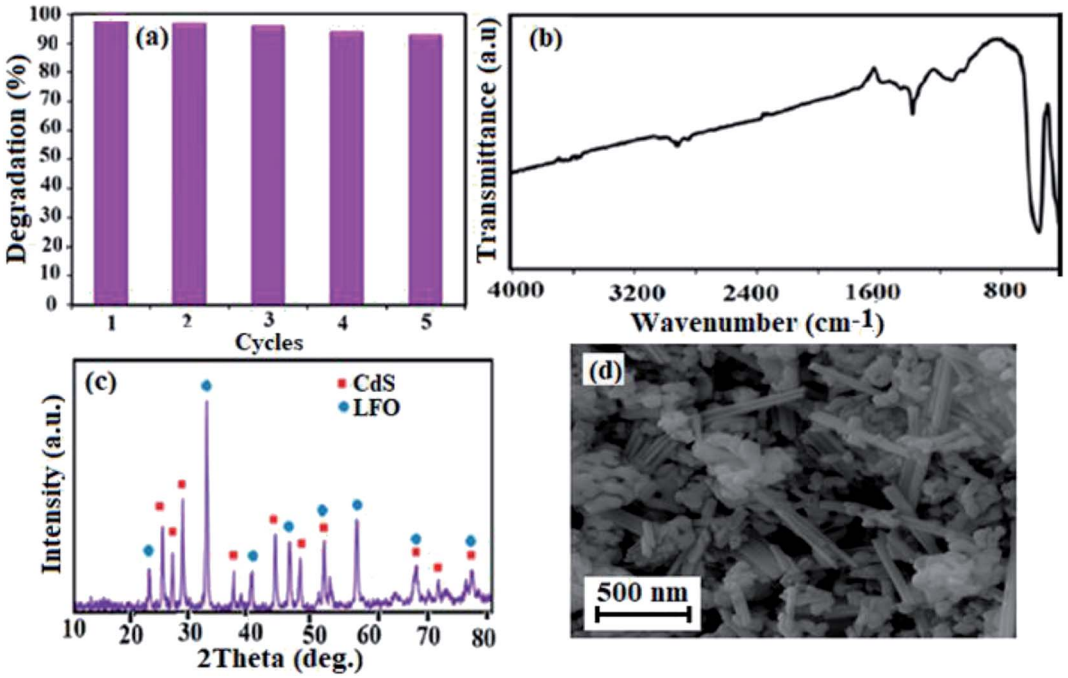

Fig. 15 (a) Recyclability tests, (b) FT-IR spectrum, (c) XRD pattern and (d) SEM image of the recovered CdS NRs/LFO photocatalyst after five runs.

emission intensity in CdS NRs/LFO nanocomposite indicates inhibition of electron–hole recombination due to the co-catalytic effect of LFO, which lengthens the lifetime of charge carriers and is beneficial for the improvement of photocatalytic activity.

3.2.6. Reusability and stability of CdS NRs/LFO. The stability of the catalyst material is one of the main advantages of the application of heterogeneous catalysts and photocatalysts in wastewater treatment. The as-synthesized nanocomposite is insoluble and can be separated from the reaction mixture by simple centrifugation, washed with water and reused for a new photodegradation experiment. The typical cycling experiments of CdS NRs/LFO were conducted to evaluate their long-term serving life, and the results are shown in Fig. 15(a). It can be clearly seen that the photocatalytic activity decreases slightly after five cycles, indicating that CdS NRs/LFO photocatalyst has a good stability. The nature of the recovered catalyst was also tested. As shown in Fig. 15(b)–(d), FT-IR, XRD and SEM analyses of the recycled CdS NRs/LFO catalyst showed no change in comparison with those of the fresh sample. These findings confirm that the structure of the CdS NRs/LFO nanocomposite is stable under the reaction conditions which are of great significance for practical application.

4. Conclusions

In summary, a novel p–n CdS NRs/LFO heterojunction composite was successfully synthesized by coupling CdS with LFO and used as a visible light photocatalyst for the degradation of organic dyes. Compared with the pristine CdS and bare LFO, the CdS NRs/LFO sample demonstrated much higher photocatalytic activity. The superior photocatalytic activity and stability of this composite were attributed to the formation of the heterojunction structure, effectively promoting the separation of photogenerated electron–hole pairs in agreement with the results of PL. Furthermore, the cycling experiments revealed the good stability of CdS NRs/LFO composite. Besides, the study on the photocatalytic mechanism of the CdS NRs/LFO heterojunction shows that ·OH radicals and h_{VB}^{+} are the participants for the degradation process of dyes. The synergistic interactions between the LFO and CdS provide a robust and novel method for combining two visible light photocatalysts to expand their visible light absorption. Meanwhile, this study provides some new insights into the design and fabrication of advanced catalysts with p–n heterojunction structures toward highly-efficient photocatalytic applications in organic pollution treatment under visible light irradiation.

Conflicts of interest

There are no conflicts of interest to declare.

Acknowledgements

The authors gratefully acknowledge the Lorestan University and Iran Nanotechnology Initiative Council (INIC) for their financial support.

References

1 A. Turki, C. Guillard, F. Dappozze, Z. Ksibi, G. Berhault and H. Kochkar, *Appl. Catal., B*, 2015, **163**, 404–414.
2 R. Saraf, C. Shivakumara, S. Behera, H. Nagabhushana and N. Dhananjaya, *Spectrochim. Acta, Part A*, 2015, **136**, 348–355.
3 F. Siadatnasab, S. Farhadi and A. Khataee, *Ultrason. Sonochem.*, 2018, **44**, 359–367.
4 J. Yan, K. Wang, H. Xu, J. Qian, W. Liu, X. Yang and H. Li, *Chin. J. Catal.*, 2013, **34**, 1876–1882.
5 M. Sheydaei and A. Khataee, *Ultrason. Sonochem.*, 2015, **27**, 616–622.
6 J. Fu, Z. Chen, M. Wang, S. Liu, J. Zhang, J. Zhang, R. Han and Q. Xu, *Chem. Eng. J.*, 2015, **259**, 53–61.
7 R. D. C. Soltani, A. Rezaee, A. Khataee and M. Safari, *J. Colloid Interface Sci.*, 2014, **20**, 1861–1868.
8 S. Farhadi, F. Siadatnasab and A. Khataee, *Ultrason. Sonochem.*, 2017, **37**, 298–309.
9 S. Li, K. Yu, Y. Wang, Z. Zhang, C. Song, H. Yin, Q. Ren and Z. Zhu, *CrystEngComm*, 2013, **15**, 1753–1761.
10 S. Cao, J. Low, J. Yu and M. Jaroniec, *Adv. Mater.*, 2015, **27**, 2150–2176.
11 M. Carrier, N. Perol, J.-M. Herrmann, C. Bordes, S. Horikoshi, J. O. Paisse, R. Baudot and C. Guillard, *Appl. Catal., B*, 2006, **65**, 11–20.
12 S. Ahmed, M. Rasul, W. N. Martens, R. Brown and M. Hashib, *Desalination*, 2010, **261**, 3–18.
13 E. Abroshan, S. Farhadi and A. Zabardasti, *Sol. Energy Mater. Sol. Cells*, 2018, **178**, 154–163.
14 W. Zhang, B. S. Naidu, J. Z. Ou, A. P. O'Mullane, A. F. Chrimes, B. J. Carey, Y. Wang, S. Y. Tang, V. Sivan, A. Mitchell, S. K. Bhargava and K. Kalantar-zadeh, *ACS Appl. Mater. Interfaces*, 2015, **7**, 1943–1948.
15 B. S. Naidu, U. Gupta, U. Maitra and C. N. R. Rao, *Chem. Phys. Lett.*, 2014, **591**, 277–281.
16 J. Yu, J. Low, W. Xiao, P. Zhou and M. Jaroniec, *J. Am. Chem. Soc.*, 2014, **136**, 8839–8842.
17 X. Wang, M. Liao, Y. Zhong, J. Y. Zheng, W. Tian, T. Zhai, C. Zhi, Y. Ma, J. Yao and Y. Bando, *Adv. Mater.*, 2012, **24**, 3421–3425.
18 S. Farhadi and F. Siadatnasab, *Chin. J. Catal.*, 2016, **37**, 1487–1495.
19 P. Gao, J. Liu, D. D. Sun and W. Ng, *J. Hazard. Mater.*, 2013, **250**, 412–420.
20 R. K. Chava, J. Y. Do and M. Kang, *Appl. Surf. Sci.*, 2018, **433**, 240–248.
21 Q. Cai, Z. Hu, Q. Zhang, B. Li and Z. Shen, *Appl. Surf. Sci.*, 2017, **403**, 151–158.
22 W. Jiang, Y. Liu, R. Zong, Z. Li, W. Yao and Y. Zhu, *J. Mater. Chem. A*, 2015, **3**, 18406–18412.
23 Z. Y. Zhang, C. L. Shao, X. H. Li, C. H. Wang, M. Y. Zhang and Y. C. Liu, *ACS. Appl. Mater. Interfaces*, 2010, **2**, 2915–2923.
24 J. Hu, Z. X. Zhong, F. Zhang, W. H. Xing, W. Q. Jin and N. P. Xu, *Ind. Eng. Chem. Res.*, 2016, **55**, 6661–6670.
25 Y. H. Ao, K. D. Wang, P. F. Wang, C. Wang and J. Hou, *Appl. Catal., B*, 2016, **157**, 168–194.

26 M. Tyagi, M. Tomar and V. Gupta, *J. Mater. Chem. C*, 2014, **2**, 2387–2393.
27 F. Schuster, B. Laumer, R. R. Zamani, C. Magen, J. R. Morante, J. Arbiol and M. Stutzmann, *ACS Nano*, 2014, **8**, 4376–4384.
28 Q. X. Zhang and J. M. Cao, *RSC Adv.*, 2015, **5**, 107957–107963.
29 P. Gao, J. C. Liu and D. D. Sun, *J. Hazard. Mater.*, 2013, **250**, 412–420.
30 Y. Feng, X. Yan and C. B. H. Liu, *Appl. Surf. Sci.*, 2015, **353**, 87–94.
31 L. Geand and J. E. Liu, *Appl. Catal., B*, 2011, **105**, 289–297.
32 Y. Cui, *Chin. J. Catal.*, 2015, **36**, 372–379.
33 Y. Ao, L. Xu, P. Wang, C. Wang, J. Hou and J. Qian, *Dalton Trans.*, 2015, **44**, 11321–11330.
34 P. Xiong, J. Zhu and X. Wang, *Ind. Eng. Chem. Res.*, 2013, **52**, 17126–17133.
35 L. Zou, H. Wang, G. Yuan and X. Wang, *ACS Appl. Nano Mater.*, 2018, **1**, 831–838.
36 C. Singh, R. Malik, V. Kumar and S. Singhal, *RSC Adv.*, 2015, **5**, 89327–89337.
37 R. K. Chava, J. Y. Do and M. Kang, *Appl. Surf. Sci.*, 2018, **433**, 240–248.
38 Q. Yu, X. Meng, T. Wang, P. Li, L. Liu, K. Chang, G. Liu and J. Ye, *Chem. Commun.*, 2015, **51**, 3630.
39 K. Xu and J. Feng, *RSC Adv.*, 2017, **7**, 45369–45376.
40 J. Yang, R. Hu, W. Meng and Y. Du, *Chem. Commun.*, 2016, **52**, 2620–2623.
41 Q. Zhang, Y. Huanga, S. Peng, Y. Zhang, Z. Shen, J. J. Cao, W. Ho, S. C. Lee and D. Y. H. Puifakey, *Appl. Catal., B*, 2017, **204**, 346–357.
42 R. D. Kumar, R. Thangappan and R. Jayavel, *J. Phys. Chem. Solids*, 2017, **101**, 25–33.
43 K. Xu, H. Xu, G. Feng and J. Feng, *New J. Chem.*, 2017, **41**, 14602–14609.
44 X. Ren, H. Yang, S. Gen, J. Zhou, T. Yang, X. Zhang, Z. Cheng and S. Sun, *Nanoscale*, 2016, **8**, 752–756.
45 S. Farhadi, M. M. Amini and F. Mahmoudi, *RSC Adv.*, 2016, **6**, 102984–102996.
46 B. M. Pirzada, P. Pushpendra, R. K. Kunchala and B. S. Naidu, *ACS Omega*, 2019, **4**, 2618–2629.
47 S. Farhadi and F. Siadatnasab, *J. Mol. Catal. A: Chem.*, 2011, **339**, 108–116.
48 R. P. Bagwe and K. C. Khilar, *Langmuir*, 2000, **16**, 905–910.
49 C. Zhao, G. Tan, J. Huang, W. Yang, H. Ren and A. Xia, *ACS Appl. Mater. Interfaces*, 2015, **7**, 23949–23957.
50 K. K. Senapati, C. Borgohain and P. Phukan, *Catal. Sci. Technol.*, 2012, **2**, 2361–2366.
51 S. Thirumalairajan, K. Girija, V. R. Mastelaro and N. Ponpandian, *New J. Chem.*, 2014, **38**, 5480–5490.
52 N. Ertugay and F. N. Acar, *Appl. Surf. Sci.*, 2014, **318**, 121–126.
53 Y. Huang, Y. Chen, C. Hu, B. Zhang, T. Shen, X. Chen and M. Q. Zhang, *J. Mater. Chem.*, 2012, **22**, 10999–11002.
54 J. He, L. Chen, F. Wang, Y. Liu, P. Chen, C. T. Au and S. F. Yin, *ChemSusChem*, 2016, **9**, 624–630.
55 L. Ge, F. Zuo, J. Liu, Q. Ma, C. Wang, D. Sun, L. Bartels and P. Feng, *J. Phys. Chem. C*, 2012, **116**, 13708–13714.
56 H. Su, L. Jing, K. Shi, C. Yao and H. Fu, *J. Nanopart. Res.*, 2010, **12**, 967–975.
57 L. L. Ju, Z. Y. Chen, L. Fang, W. Dong, F. G. Zheng and M. R. Shen, *J. Am. Ceram. Soc.*, 2011, **10**, 3418–3424.
58 W. Luo, L. H. Zhu, N. Wang, H. Q. Tang, M. J. Cao and Y. B. She, *Environ. Sci. Technol.*, 2010, **44**, 1786–1791.
59 L. Li and X. Wang, *J. Sol-Gel Sci. Technol.*, 2016, **79**, 107–113.
60 H. C. Lan, A. M. Wang, R. P. Liu, H. J. Liu and J. H. Qu, *J. Hazard. Mater.*, 2015, **285**, 167–172.
61 S. Farhadi and F. Siadatnasab, *Mater. Res. Bull.*, 2016, **83**, 345–353.
62 R. Liang, S. Luo, F. Jing, L. Shen, N. Qin and L. Wu, *Appl. Catal., B*, 2015, **176**, 240–248.
63 N. Z. Bao, L. M. Shen, T. S. Takata and K. Domen, *Chem. Mater.*, 2008, **20**, 110–117.
64 F. Akbal, *Environ. Prog.*, 2005, **24**, 317–322.
65 N. Guettaï and H. Ait Amar, *Desalination*, 2005, **185**, 427–437.
66 M. R. Gholipour, C. T. Dhin and T. O. Do, *Nanoscale*, 2015, **7**, 8187–8208.
67 W. J. Li, D. Z. Li, J. X. Wang, Y. Shao, J. M. You and F. Teng, *J. Mol. Catal. A: Chem.*, 2013, **380**, 10–17.
68 Y. Chen, G. Tian, Y. Shi, Y. Xiao and H. Fu, *Appl. Catal., B*, 2015, **164**, 40–47.
69 X. K. Li, N. Kikugawa and J. H. Ye, *Adv. Mater.*, 2008, **20**, 3816–3819.
70 H. Y. Ji, X. C. Jing, Y. G. Xu, J. Yan, H. P. Li, Y. P. Li, L. Y. Huang, Q. Zhang, H. Xu and H. M. Li, *RSC Adv.*, 2015, **5**, 57960–57967.
71 J. Zeng, T. Song, M. X. Lv, T. T. Wang, J. Y. Qin and H. P. Zeng, *RSC Adv.*, 2016, **6**, 54964–54975.
72 D. D. Lv, D. F. Zhang, X. Y. Liu, Z. G. Liu, L. Y. Hu, X. P. Pu, H. Y. Ma and D. C. Li, *Sep. Purif. Technol.*, 2016, **158**, 302–307.
73 P. Xiong, Y. S. Fu, L. J. Wang and X. Wang, *J. Chem. Eng.*, 2012, **195–196**, 149–157.
74 H. Y. Zhu, R. Jiang, Y. Q. Fu, R. R. Li, J. Yao and S. T. Jiang, *Appl. Surf. Sci.*, 2016, **369**, 1–10.
75 L. Zhang and W. L. Jiao, *J. Alloys Compd.*, 2013, **581**, 11–15.
76 J. Zhou, L. Yin, K. Zha, H. R. Li, Z. Y. Liu, J. X. Wang, K. Duan and B. Feng, *Appl. Surf. Sci.*, 2016, **367**, 118–125.
77 M. N. Ha, F. Zhu, Z. F. Liu, L. C. Wang, L. Y. Liu, G. Z. Lu and Z. Zhao, *RSC Adv.*, 2016, **6**, 21111–21118.
78 D. Yang, Y. Y. Sun, Z. W. Tong, Y. H. Nan and Z. Y. Jiang, *J. Hazard. Mater.*, 2016, **312**, 45–54.
79 O. Ruzimuradov, M. Hojamberdiev, C. Fasel and R. Riedel, *J. Alloys Compd.*, 2017, **699**, 144–150.
80 D. Wang, G. Xue, Y. Zhen, F. Fub and D. Li, *J. Mater. Chem.*, 2012, **22**, 4751–4758.
81 D. Wang, L. Guo, Y. Zhen, L. Yue, G. Xue and F. Fu, *J. Mater. Chem. A*, 2014, **2**, 11716–11727.
82 Y. J. Yuan, D. Q. Chen, Y. W. Huang, Z. T. Yu, J. S. Zhong, T. T. Chen, W. G. Tu, Z. J. Guan, D. P. Cao and Z. G. Zou, *ChemSusChem*, 2016, **9**, 1003–1009.
83 T. H. Yu, W. Y. Cheng, K. J. Chao and S. Y. Lu, *Nanoscale*, 2013, **5**, 7356–7360.
84 Y. Xia, Z. He, Y. Lu, B. Tang, S. Sun, J. Su and X. Li, *RSC Adv.*, 2018, **8**, 5441–5450.

85 Y. Jin, X. Shen, Z. Liu, Z. Wang, B. Zhu, P. Xu, L. Luo and L. Zhang, *New J. Chem.*, 2018, **42**, 411–419.
86 S. W. Zhang, H. C. Yang, H. H. Gao, R. Cao, J. Z. Huang and X. J. Xu, *ACS Appl. Mater. Interfaces*, 2017, **9**, 23635–23646.
87 W. Cui, W. An, L. Liu, J. Hu and Y. Liang, *Appl. Surf. Sci.*, 2014, **319**, 298–305.
88 Y. Xia, Z. He, J. Su, B. Tang, K. Hu, Y. Lu, S. Sun and X. Li, *RSC Adv.*, 2018, **8**, 4284–4294.